Terahertz Plasmonic Excitations in Bi_2Se_3 Topological Insulator

M. Autore,[1] P. Di Pietro,[2] A. Di Gaspare,[3] F. D'Apuzzo,[4] F. Giorgianni,[5]
Matthew Brahlek,[6] Nikesh Koirala,[6] Seangshik Oh,[6] and S. Lupi[5]

[1]*INFN and Dipartimento di Fisica, Università di Roma "La Sapienza", Piazzale A. Moro 2,*
I-00185 Roma, Italy, and CIC nanoGUNE Tolosa Hiribidea, 76 E-20018 Donostia San Sebastian, Spain
[2]*Elettra - Sincrotrone Trieste S.C.p.A. S.S. 14 Km 163,*
5 in AREA Science Park IT-34149 Basovizza, Trieste, Italy
[3]*NEST, Istituto Nanoscienze-CNR and Scuola Normale Superiore, Piazza S. Silvestro 12, 56127 Pisa, Italy*
[4]*Affiliate - Advanced Light Source (ALS) Division Lawrence Berkeley National*
Laboratory 1 Cyclotron Road, MS 7R0222 Berkeley, CA 94720, USA
[5]*INFN and Dipartimento di Fisica, Università di Roma "La Sapienza", Piazzale A. Moro 2, I-00185 Roma, Italy*
[6]*Department of Physics and Astronomy Rutgers,*
The State University of New Jersey 136 Frelinghuysen Road Piscataway, NJ 08854-8019 USA
(Dated: February 22, 2017)

After the discovery of Dirac electrons in condensed matter physics, more specifically in graphene and its derivatives, their potentialities in the fields of plasmonics and photonics have been readily recognized, leading to a plethora of applications in active and tunable optical devices. Massless Dirac carriers have been further found in 3-dimensional (3D) topological insulators (TI). These exotic quantum systems have an insulating gap in the bulk and intrinsic Dirac metallic states at any surface, sustaining not only single-particle excitations but also plasmonic collective modes. In this paper we will review the plasmon excitations in different microstructures patterned on Bi_2Se_3 topological insulator thin films as measured by terahertz spectroscopy. We discuss the dependence of the plasmon absorption versus the microstructure shape, wavevector, and magnetic field. Finally we will discuss the topological protection of both the Dirac single-particle and plasmon excitations.

INTRODUCTION

During the last decades, the field of plasmonics has been object of extensive research, as a potential technological platform to combine electronics and photonics at the nanoscale. Plasmons are collective oscillations of charge carriers in metal and semiconductors, that can propagate over extended surfaces or can be localized as eigen-mode of an engineered nanostructure, thus enabling subwavelength light confinement and a giant electric field enhancement into specific nano-sized regions, called hotspots [1]. These appealing properties have been proved to be an excellent tool in a wide range of applications, such as optical sensing [2–8], quantum electrodynamics [9, 10], nonlinear optics [11, 12], photovoltaic technologies [13], and medical diagnosis and treatment [14, 15]. Many efforts have been made to engineer plasmonic devices with tailored plasmon frequencies and associated electric field spatial distribution. This can be achieved by fabricating different metallic micro- and nanostructures [16, 19–26] and exploiting widely studied phenomena as Fano interactions [17, 18] with other excitations, plasmon hybridization [27, 28], and electromagnetically induced transparency [29, 30].
Nevertheless, there is growing awareness inside the scientific community that the full potential of this field has still to be realized. To this extent, one of the key points is the investigation and development of new plasmonic materials able to improve the plasmonic performance, in particular in the mid-infrared and terahertz parts of the electromagnetic spectrum. Plasmonic devices have been indeed conventionally based on noble metals, which suffer from many drawbacks, such as losses [31, 32], high carrier concentration leading to scarce tunability and difficulty with incorporation into silicon based platforms [33]. So far, several alternative plasmonic materials have been studied, such as low and high-Tc superconductors [29], conductive oxides [33], and graphene [28, 34–40]. In particular, graphene shows an unprecedented potential in electro-optical applications, due to its peculiar electronic structure characterized by Dirac electrons.

The total energy for a relativistic particle of rest mass m can be written as $E = \pm\sqrt{p^2c^2 + m^2c^4}$. For a particle with zero rest mass, this equation reduces to $E = \pm pc$, and the particle follows the massless Dirac equation, with linear energy/momentum dispersion. The existence in solid-state physics of particles showing this behavior has just recently been proved in graphene and its derivatives, whose electrons indeed show linear dispersion relation and a zero density of states at the Fermi energy.

This means that a few additional charge carriers produce a large shift in the chemical potential strongly modulating the optical properties of graphene and plasmon-based graphene devices, providing excellent levels of electro-optical tuneability *via* chemical and/or electrostatic doping [41–43].

Besides graphene, Dirac charge carriers have been successively discovered in three-dimensional topological insulators. These exotic quantum systems are intrinsically stratified materials characterized, in the bulk, by an insulating electronic gap due to a strong spin-orbit interaction (SOI), and by gapless Dirac surface states at any edge and interface [44–46]. They thus provide a 2D Dirac-fermion system segregated from the bulk material without the need of physically implementing an atomic monolayer, as in the case of graphene. Moreover, TI surface states show other peculiar properties, such as spin-momentum locking and back-scattering protection by time-reversal symmetry. This means that they cannot be destroyed or gapped by scattering processes, other than magnetic impurities. Because of these appealing features, TIs have attracted a growing interest due to their potential application in quantum computing [47, 48], terahertz (THz) detectors [49], and spintronic devices [50], and some of these applications could benefit from propagating and localized plasmons in these materials. Moreover, the spin-momentum locking of the Dirac electrons theoretically lead to a coupling between the plasmon modes and the spin waves, giving rise to the so-called *spin-plasmon* excitations [51]. This coupling, in principle, could provide a control of the spin excitations through the electromagnetic field.

2D Dirac electrons at the surface of topological insulators have been proved to sustain both single-particle [52] and plasmon excitations [53–57]. In this paper we will review the plasmonic excitations in Bi_2Se_3 topological insulator thin films. Among TIs, Bi_2Se_3 is one of the most promising materials because of the large bulk gap $E_g \simeq 300$ meV which reduces extrinsic effects due to surface contamination and unstoichiometry [58].

This paper is organized as follows: In Section 1 we discuss the crystal and electronic structures of Bi_2Se_3. Fabrication procedure of Bi_2Se_3 thin films and plasmonic microstructures will be discussed in Section 2. In Section 3 we will provide information about THz spectroscopy experimental technique. In Section 4 we review plasmon excitations in different patterned structures: ribbon array and ring array of different pitch and particle size. In Section 5 the ribbon structures will be studied versus a strong magnetic field in order to investigate magnetoplasmon excitations. In Section 6, we will discuss the effect of topological protection on single-particle and plasmons in Bi_2Se_3. Finally, in Section 7, we conclude the paper suggesting some perspectives on plasmonics in 3-Dimensional topological insulators.

1. CRYSTAL AND ELECTRONIC STRUCTURE OF BI$_2$SE$_3$.

After its theoretical prediction in 2009 [59], it was rapidly demonstrated that bismuth selenide (Bi_2Se_3) rep-

resents a prototypical strong 3D topological insulator. Indeed, its discovery promotes many new technological applications, mostly because its topological behavior persists even at room temperature. Moreover, Bi_2Se_3 has a relatively large semiconducting gap of nearly 300 meV and a single Dirac cone with a single band inversion at the Γ point, at variance with other 3D topological insulators characterized by several surface bands. The crystalline structure of this material is rhombohedral (point group $\bar{3}mD_3d$ [60]), with five atoms per unit cell. As it is shown in Fig.1, the structure is layered characterized by a triangular lattice. The unit structure is constituted by a *quintuple layer* (QL) which consists of five atoms with two equivalent Se atoms, two equivalent Bi atoms and a third Se atom, denoted Se_1, Se_1, Bi_1, Bi_1 and Se_2, as shown in Fig.1, respectively. QLs are oriented perpendicularly to the vertical axis, and the van der Waals force between two different QLs is much weaker than the covalent bonding within each QL. The Se_2 site corresponds to an inversion centre of symmetry that enables to construct eigenstates with definite parity for the system. The total thickness of Bi_2Se_3 is always an integer number of quintuple layers, hence the film grows up by a stacking of Bi-Se QLs, which are approximately 1 nm thick.

A strong spin-orbit interaction (SOI) is at the origin of the band inversion in Bi_2Se_3 [59]. The band structure at the Γ point of Bi_2Se_3 can be built through three hybridization steps, which are represented in Fig. 2a. The first step is the chemical bonding between atoms within a QL. The second step is the crystal-field splitting and the third one is obtained by adding the SOI, that is responsible of the crossing of the Bi and Se bands. Indeed, the energy position of the states $P1_z^+$ and $P2_z^-$ depends on the SOI intensity. If the SOI is large enough, their energy position is reversed. As these two bands have an opposite parity, their inversion drives the system into a topological insulating phase. In the energy-momentum-space this is described by the sketch in Fig. 2b. The insulating bulk is characterized by a valence band separated by a gap from the conduction band. The bulk states are spin-degenerate, that is $E(\mathbf{k},\uparrow) = E(-\mathbf{k},\downarrow)$ and $E(\mathbf{k},\uparrow) = E(-\mathbf{k},\uparrow)$, because of time-reversal and space symmetries. At any interface, space inversion symmetry is violated and spin-splitting occurs due to the SOI, except at Time-Reversal-Invariant-Momentum points (Kramers points). Hence, spin-momentum locked surface states start from the bulk valence band, cross each other at Γ (the only Kramers point in Bi_2Se_3) and merge with the bulk conduction band. These surface states show a linear energy/momentum dispersion E(k)=$v_F\hbar$k corresponding to massless fermions, as described above.

However, as usually in small gap semiconductors, band-bending effects and surface accumulation layers may induce massive electrons at the Bi_2Se_3 surface [58]. Terahertz measurements on the same films we investi-

gated in this paper, have further shown that those massive electrons participate to surface conduction with a small contribution, less than 10% with respect to the total surface carrier density [52]. In the following we will discuss the plasmonic excitations at the surface of Bi_2Se_3 thin films and we will show that Dirac carriers provide the main contribution to these excitations.

2. FILM GROWTH AND FABRICATION PROCEDURE OF BI₂SE₃ MICROSTRUCTURES.

High-quality thin films of Bi_2Se_3 were prepared by molecular beam epitaxy using the standard two-step growth method developed at Rutgers University [58, 61]. 10×10 mm² Al_2O_3 substrates were first cleaned by heating to 750 °C in an oxygen environment to remove organic surface contamination. The substrates were then cooled to 110 °C, and an initial three quintuple layers of Bi_2Se_3 were deposited. This was followed by heating to 220 °C, at which the remainder of the film was deposited to achieve the target thickness. The Se:Bi flux ratio was kept to ∼10:1 to minimize Se vacancies. Bi_2Se_3 microstructures were fabricated by electron-beam lithography and subsequent reactive ion etching at the CNR-IFN institute in Rome. The Bi_2Se_3 film microstructure patterns were then written in the resist (PMMA) by electron-beam lithography. To obtain a lithographic pattern with a realignment precision below 10 nm over a sample area suitable for terahertz spectroscopy of 10×10 mm², we used an electron beam writer equipped with an x-y interferometric stage (Vistec EBPG 5000). The patterned resist served as mask for the removal of Bi_2Se_3 by reactive ion etching at a low microwave power of 45 W to prevent heating of the resist mask. Sulphur hexafluoride (SF_6) was used as the active reagent. The Bi_2Se_3 films were etched at a rate of 20 nm min^{-1}, which was verified by atomic force microscopy after soaking the sample in acetone to remove the PMMA. The in-plane edge quality after reactive ion etching, inspected by atomic force microscopy, closely follows that of the resist polymer mask, that is, with an edge roughness of <20 nm. Examples of fabricated microstructures are presented in Fig. 3 where we show both ribbon and ring arrays.

3. TERAHERTZ SPECTROSCOPY EXPERIMENTAL TECHNIQUE.

We measure the light intensity transmitted by uniform films and microstructures by steady-state terahertz spectroscopy (1 THz=33 cm^{-1}=300 μm=4 meV). The transmitted intensity I_s, normalized to that of a bare substrate I_0, provides the transmittance T(ν)=I_s/I_0 [53–56]. From T(ν) we determine the extinction coefficient E(ν)=1-T(ν) whose behavior versus microstructure shape, size

and magnetic field will be discussed in the following sections. Measurements in high magnetic fields have been performed at the High Field Magnet Laboratory in Nijmegen (The Netherlands) using a Bruker IFS113v spectrometer coupled to a resistive magnet. Light propagated parallel to the magnetic field direction and perpendicular to the sample surface (Faraday geometry), and the magnetic field was varied from 0 to 30 T, with 2.5 T steps.

4. PLASMON EXCITATIONS IN PATTERNED STRUCTURES OF BI₂SE₃.

The plasmon dispersion law is such to prevent the conservation of momentum in a photon absorption process. The extramomentum necessary to activate the absorption can be obtained by patterning the sample surface with a subwavelength structure [62, 63]. A qualitative example of plasmon dispersion is shown in Fig.4 and the extramomentum for an array of ribbons is represented in the inset of the same Figure.

In this paper we will discuss the plasmon modes of different micro-structures: an array of one-dimensional (1D) ribbons and an hexagonal array of circular rings.

4a. Ribbon array

The arrays of parallel ribbons are shown in Fig.5. Here the array period is $L = 2W$ and the ribbon width W. This determines an extrawavevector of $k = \pi/W$ and a filling factor of the structure equal to 0.5. In Fig. 5a the Scanning Electron Microscope (SEM) image of the W=2.5 μm patterned film is shown. Let us note that the ribbon-array structure shows an intrinsic optical anisotropy. For ligth polarization perpendicular to ribbons, plasmon can be excited, while through the parallel polarization one probes the single-particle optical response of Dirac electrons.

The extinction coefficient $E(\nu)$ of ribbon-array is reported in Fig 5b at T= 6 K, for a uniform (non-patterned) film and for the patterned films (d,e), once normalized by the respective peak values at 6 K (black lines). The uniform film in Fig. 5b exhibits a phonon peak absorption (α mode) at 1.85 THz (61 cm^{-1}) and a barely observable β mode at 4.0 THz (132 cm^{-1}) [64]. These modes, characteristic of the insulating bulk, are superimposed to a Drude absorption, which is mainly related to Dirac surface states [52] (see also discussion below). $E(\nu)$ of the patterned samples is reported in Fig. 5d for the radiation electric field $\vec{E}$ parallel to the ribbons. Therein, the phonon frequencies neither appreciably change with W, nor with film thickness t. Moreover, spectra are very similar to that in Fig. 5b. This indicates that the patterning procedure do not affect the physical and chemical properties of films and one probes,

along this polarization direction, the single-particle carrier excitations.

Fig. 5e shows instead the extinction coefficient for a polarization perpendicular to the ribbons, *i.e.* along the polarization direction where the plasmon can be excited. As one can see, the α phonon is replaced by a double absorption, where both peak frequencies strongly depend on W. These features are due to a mutual interaction among the α phonon and the plasmon via a Fano interference. This interaction produces a renormalization of both excitation frequencies and a reshaping of the whole absorption, with a hardening of the mode at higher frequency and a softening of that at lower frequency, independently of their nature. A similar effect has been reported in the literature for the interaction among doped graphene and the mid-infrared phonon of SiO_2 substrate [65].

In order to extract from the data in Fig. 5e the bare plasmon (ν_p) and phonon (ν_{ph}) frequencies, we have fitted the experimental data to a Fano model, obtained by Giannini et al. [66]:

$$E(\nu') = \frac{(\nu' + q(\nu'))^2}{\nu'^2 + 1} \cdot \frac{g^2}{1 + \left(\frac{\nu - \nu_p}{\Gamma_p/2}\right)^2} \qquad (1)$$

The expressions for the renormalized frequency ν' and for the Fano parameter q, that is the ratio between the probability amplitude of exciting a discrete state (phonon) and a continuum state (plasmon) are the following:

$$\nu' = \frac{\nu - \nu_{ph}}{\Gamma_{ph}(\nu)/2} - \frac{\nu - \nu_P}{\Gamma_p/2} \qquad (2)$$

$$q(\nu) = \frac{vw/g}{\Gamma_{ph}(\nu)/2} + \frac{\nu - \nu_P}{\Gamma_p/2} \qquad (3)$$

where the plasmon-coupled phonon linewidth is:

$$\Gamma_{ph}(\nu) = \frac{2\pi v^2}{1 + \left(\frac{\nu - \nu_p}{\Gamma_p/2}\right)^2} \qquad (4)$$

Therein, w and g are the coupling factors of the radiation with the phonon and the plasmon, respectively, v measures the phonon-plasmon interaction, and Γ_p is the width of the plasmon line, assumed to be Lorentzian. Finally, ν_p is the plasmon bare frequency (see Ref. [53] for more details).

The above model satisfactorily reproduces the experimental data (red-empty circles) as shown by the dashed black-line in Fig. 6. Therein, the bare phonon (blue line) and plasmon (green line) contributions are also shown. The phonon frequency does not change with W being the same as in Fig. 5d (parallel polarization) while, for

the plasmon, both ν_p and Γ_p decrease as W increases (see also the inset in the bottom panel of Fig. 6).

The bare plasmon frequencies ν_p obtained from the Fano fits are plotted *vs.* the experimental wavevector $k = \pi/W$ in Fig. 7. In order to assign the plasmon excitations at the surface of Bi_2Se_3 to Dirac carriers we compare in Fig. 7 the experimental dispersion law (red circles) with theory. In particular, in Fig. 7 we plot the Dirac dispersion (blue-dashed line), which, in the long wavelength limit $k \to 0$ can be written as [67, 68]:

$$\nu_D(k) = \frac{1}{2\pi}\sqrt{k}\left(\frac{e^2}{4\pi\epsilon_0\epsilon\hbar}v_F\sqrt{2\pi n_D}\right)^{1/2} \qquad (5)$$

In Bi_2Se_3 thin films $n_D = 3 \pm 1 \times 10^{13}$ cm^{-2}, $v_F = 6 \pm 1 \times 10^7$ cm/s [69]. It is worth to note that Eq. 5 does not contain (in this low-k limit) either the film thickness and the bulk dielectric function. It instead depends on the average $\epsilon = (\epsilon_1 + \epsilon_2)/2$ between the vacuum dielectric function ($\epsilon_1 = 1$) and that of the substrate ($\epsilon_2 \sim 10$). The theoretical dispersion was calculated by Eq. 5 at the wavevectors $k = \pi/W$ by using for n_D, v_F, their experimental values reported above. Calculation is reported in Fig. 7 (blue dashed line) and one finds a very good agreement with the experimental data (red circles), without using free parameters.

In Refs. [70, 71], however, it has been noted that at the highest wavevectors we measured, the low-k limit Equation (Eq. 5) is inadequate to describe experimental data. The authors of Ref. [70] proposed to modify Eq.5 with a corrective term which contains the bulk dielectric function ϵ_{bulk} of Bi_2Se_3 and shows an explicit dependence on the film thickness t.

$$\nu_D(k) = \frac{1}{2\pi}\sqrt{k}\left(\frac{e^2}{4\pi\epsilon_0\epsilon\hbar}v_F\sqrt{2\pi n_D}\right)^{1/2}[1 + \frac{kt\epsilon_{bulk}}{2\epsilon}]^{-1/2} \qquad (6)$$

In Ref. [70, 71] the calculation has been performed by assuming ϵ_{bulk}=100 as measured in the mid-infrared range in Bi_2Te_3 single-crystals [60] and using the same parameters (Fermi velocity, surface Dirac charge density, and dielectric functions at the film interfaces), as made in Eq. 5. Results are reported in Fig. 7 by black line and red line for film thickness of 60 QL and 120 QL, respectively. As well evident, Eq. 6 (for ϵ_{bulk}=100) does not describe plasmon frequency data in the whole range of wavevectors representing, actually, a strong underestimate of the experimental results. Calculations have been also made by assuming ϵ_{bulk}=30, a value which is more representative of dielectric properties of nearly stoichiometric Bi_2Se_3 single crystals [64]. In this case (red and black dashed lines in Fig. 7), a small discrepancy still exists, in particular at high wavevectors, although it is strongly reduced with respect to calculation for ϵ_{bulk}=100.

In order to clarify better the dielectric properties of the Bi_2Se_3 bulk which enters in Eq. 6, we have measured reflectance and transmittance of our films grown on sapphire substrate from 500 to 6000 cm^{-1} and we have extracted the real part of the bulk dielectric function in the same spectral range through a Kramers-Kronig consistent fit [72]. ϵ_{bulk} can be estimated in this frequency region as Stauber et al made in Ref. [70]. As shown in the inset of Fig. 7, ϵ_{bulk} is nearly constant, assuming an average value ~ 22 between 500 to 6000 cm^{-1}. This experimentally demonstrates that bulk $\epsilon_{bulk} = 30$ as obtained in nearly stoichiometric Bi_2Se_3 single crystal is an overestimate of the actual value, and $\epsilon_{bulk} = 100$ as reported in Ref. [70] (measured on non stoichiometric controlled Bi_2Te_3 single crystals and then subject to spurious contributions), is absolutely not consistent with our films.

Eq. 6 has been calculated for $\epsilon_{bulk} = 22$ for the actual film thickness and the result is represented in Fig. 7 by green diamonds. A good agreement is achieved between theory and experimental data in this case. The small disagreement (underestimate), less than 10% at the highest wavevector, could indicate a possible small role of massive electrons at the surface of Bi_2Se_3.

A plasmonic response due to massive carriers has been recently observed via High Resolution Electron Energy Loss spectroscopy (HREELS) [57] in Bi_2Se_3 single crystals at room temperature and high wavevectors, and its interplay with the Dirac plasmon has been studied. Let us observe, however, that this experiment has been performed on Bi_2Se_3 single crystals where the bulk conductivity is strongly affected by impurities and out-of-stoichiometry Bi:Se ratio [64]. These spurious contributions cannot be completely reduced even in more compensated materials like $Bi_2(Se_{1-x}Te_x)_3$ [64]. Moreover, this bulk non compensation reflects into an excess of massive carriers at the surface in particular at room temperature where most of impurities are ionized and where HREELS measurements have been performed. So, although the results of [57] are very interesting, they cannot directly be compared with optical data collected at He temperature on better compensated thin films grown by MBE techniques.

The optical detection of the massive conduction channel in the THz range is still object of investigation and has led, so far, to different results: in Ref. [52, 55, 83] authors report optical conductivity data and fit them to a Drude-Lorentz model with a single Drude term (with a scattering rate $\Gamma < 1.5$ THz), finding a good quantitative agreement between the extracted Drude spectral weight and the Dirac carrier density measured via transport. This analysis led to the conclusion that the massive carriers contribution is at least negligible at low temperatures in the THz range, where therefore the corresponding conductance determining the plasmon response is mainly due to Dirac carriers. On the other side, in

Ref. [73] the authors fit similar data to a model with two different Drude terms: A narrow contribution ($\Gamma < 1.5$ THz), related to Dirac carriers, and another broad term ($\Gamma > 4$ THz), related to massive carriers. The massive Drude provides a small, less then 10%, contribution to the total Drude spectral weight. Let us notice, that this value ($\sim 10\%$) is in good agreement with that estimate from Fig. 7 at the highest wavevector. Nevertheless, the massive carriers contribution has been showed to play an important role in out of equilibrium dynamics of THz TIs plasmons, as probed via pump probe experiments [74]. Therefore, although we cannot exclude a contribution of surface massive electrons both to single-particle and plasmon excitations of Bi_2Se_3 thin films, in the present situation this contribution cannot be larger than 10% of the total density of carriers. So, we can ascribe the plasmon excitations mainly to Dirac carriers.

4b. Ring array

One of the interesting aspects of plasmonics, is the possibility to implement and study the interaction and hybridization of plasmonic modes in complex nanostructures [27]. This can be achieved for instance in micro-ring arrays, which offer a richer plasmonic spectrum compared to a parallel ribbon array [26, 54]. The plasmon modes in a ring can be understood according to the scheme shown in Fig. 8b: a ring is the superposition of a disk and an anti-dot, which both sustain dipolar plasmonic excitations. The superposition of the two modes leads to their hybridization, into bonding and antibonding modes, the first (at lower frequency) corresponding to a symmetric charge fluctuation across the ring and the second (at higher frequency) related to an antisymmetric charge distribution. In order to investigate the ring micro-structure, four films of Bi_2Se_3 (thickness t=60 nm) were patterned by electron-beam lithography and reactive-ion etching to form periodic hexagonal arrays of rings with different sizes. The outer (D) and inner (d) ring diameters were chosen to have a D/d=3 disk-to-hole aspect ratio, while the ratio between the lattice period and the inner diameter was taken approximately to be a/d=4 for all samples. Fig. 8a shows a scanning electron microscope (SEM) image of the D=15 μm patterned film, whereas Fig. 8c presents optical microscope images of the different arrays.

The extinction spectra of the ring-arrays, shown in Fig. 8d at 10 K (solid lines), exhibit a three peak structure which shifts to higher frequency (blue shift) as the ring size is decreased. These spectral features can be explained by considering the fundamental bonding and antibonding plasmon excitations of a ring and their Fano interaction with the α phonon (see Fig. 8b). In Bi_2Se_3 microrings, the bonding mode interacts via a Fano process with the α phonon at 1.85 THz (similarly to what

happens in the ribbon-array), determining the characteristic peak-to-dip structure at low-frequency. The antibonding plasmon is instead always at higher frequency to the phonon mode (at least for the geometrical parameters here considered) and shows a negligible interaction with the phonon.

In order to quantitavely investigate this behavior, theoretical electromagnetic simulations have been performed, according to a model based on the polarizability of thin scatterers, previously reported in several works [28, 75]. In this model, the only material parameter is the terahertz conductance of unpatterned Bi_2Se_3 film, which was measured in films coming from the same batch. The resulting spectra are reported in Fig. 8d (dashed lines) and show an overall good agreement with experimental data. An useful insight into the observed phenomena is presented in Fig. 9, were the measured bonding and antibonding plasmon modes, together with the α-phonon (i.e. the corresponding maxima of extinction in Fig. 8d) are reported as blue, red and black circles, respectively, as a function of $1/D$, a parameter proportional to the "effective extrawavector" needed to activate the photon absorption process. The dispersion of the observed modes is compared in the same figure to their bare theoretical dispersion in the absence of the plasmon-phonon interaction (occurring between bonding mode and α-phonon), obtained by artificially switching off the phonon mode in the electromagnetic simulations. The bare bonding mode (blue dashed line) crosses the phonon frequency (black dashed horizontal line) and these two modes hybridize, giving rise to extinction maxima above and below the phonon line (and a minimum around the bare phonon frequency in agreement with the Fano mechanism). In contrast, the bare antibonding plasmon (red dashed line) is always far away to the phonon frequency, so that its dispersion only experiences a mild redshift due to interaction with the latter.

These two examples of patterning structures show an intrinsic richness of the terahertz plasmon excitation spectrum on the Bi_2Se_3 surface. This richness is due to the high surface density of Dirac carriers in combination with the Fano interaction of plasmon modes with the phonon spectrum of TIs whose characteristic frequencies are in the terahertz range both in Bi_2Se_3 and in the other 3D TI families.

5. MAGNETOPLASMON EXCITATIONS IN Bi_2Se_3.

In the previous Sections we have studied the plasmon excitations in Bi_2Se_3 topological insulator films vs. the geometrical shape: micro- ribbons and rings. However, the excitations of a 2D electron gas are also sensitive to the presence of an external magnetic field B [76]. In particular, the single-particle optical response described by

a Drude mode at zero field shifts at finite frequency for B>0 due to the excitation of a cyclotron resonance. A similar hardening happens also for plasmon excitations. At zero field, in a ribbon-array, a single plasmon mode is present (see Section 3a). In the following we will show that this mode transforms into a magnetoplasmon excitation which shifts to higher frequency vs. B and whose dispersion vs B superimposes to the cyclotron dispersion at high field B. The evolution with B of both cyclotron resonance and magnetoplasmon will be used in the following to achieve two independent estimate of the dynamical mass of Dirac carriers in Bi_2Se_3 thin films.

In Fig. 10 we show the extinction coefficient $E(\nu)$ vs. frequency at different magnetic fields B (from 0 to 30 T) for light polarization both perpendicular (plasmon, left panel) and parallel (single-particle, right panel) to ribbons. Subsequent increasing field spectra are offset by a factor +0.1 to better display the behavior of excitations. At zero field the perpendicular polarization shows the plasmon Fano hybridization with the α-phonon giving rise to the peak-to-deep structure (Fig. 10, left panel) as discussed in Section 3a. The Drude term corresponding to the single-particle Dirac excitations superimposed to the α mode can be instead observed for the parallel polarization (Fig. 10b). The plasmon mode evolves with B into a unique excitation, as effect of the combination between plasmon and cyclotron resonance. This new mode, called magnetoplasmon, still shows a Fano interaction with the α phonon at any magnetic field value [56]. On the other hand the Drude term evolves into a finite frequency mode for B>0, i.e. the cyclotron resonance. The bare magnetoplasmon frequency ν_{mp} (orange-squares) at all the measured B values is extracted from a Fano fit (see Section 3a) of the corresponding extinction coefficient. The cyclotron frequency ν_c (green-circles) is instead determined fitting the corresponding spectra according to the standard cyclotron resonance model for conductivity [77] plus a lorentzian which captures the α phonon mode.

Both the bare plasmon and the cyclotron modes are plotted in Fig. 11 vs. the magnetic field B.

The magnetoplasmon frequency ν_{mp} follows the equation [78]

$$\nu_{mp} = \sqrt{\nu_p^2 + \nu_c^2} \qquad (7)$$

where ν_p is the plasmon frequency at zero field and ν_c is the cyclotron frequency for the surface Dirac carriers. As in our films the Fermi energy is $E_F \simeq 400$ meV, well above the Dirac point, the cyclotron resonance takes the following classical dependence on the magnetic field

$$\nu_c = \frac{eB}{2\pi m^*} \qquad (8)$$

Therefore, through Eq. 6 and 7, one can fit the behavior of both the magnetoplasmon and cyclotron frequen-

cies *vs.* the magnetic field B. These fits (orange and green dashed lines, respectively), where the only free parameter is the dynamical mass of Dirac carriers m^*, provide a value of $m^*=0.18\pm0.01$ m$_e$ (m$_e$ is the bare electron mass), for both the magnetoplasmon and cyclotron resonance magnetic B dependence.

From Fig.11 one observes, at low field, that the cyclotron resonance is still well separated in energy from the magnetoplasmon mode. At higher fields both excitations asymptotically converge at the same energy, giving rise to a universal Dirac magnetic excitation on the surface of Bi$_2$Se$_3$.This behavior demonstrates an excellent magnetic control of electronic excitations in TIs, and this could open the way towards plasmon controlled (terahertz) magneto-optics devices [79].

Plasmon modes in topologically more complex structures like TI micro-rings have not been investigated so far in a magnetic field. Here, theory [80] suggests a non trivial behavior with the presence of excitations resembling the bonding and the antibonding modes previous discussed at zero field (Section 3b), and the appearence of edge modes at finite B, *i.e.* 1D excitations, propagating around the short and long ring diameters. Further work should be dedicated to investigate these exotic plasmons in rings and in other structures of topological insulators.

6. TOPOLOGICAL PROTECTION OF SINGLE PARTICLE AND PLASMON MODES.

Dirac surface carriers are a consequence of the non trivial topology of Bi$_2$Se$_3$ 3D topological insulator [59]. As introduced above, these carriers are intrinsically protected from backscattering in absence of magnetic impurities. This property is particularly appealing for applications, because topological protection should reflect in reduced transport losses and single-particle and plasmon observability even at room and higher temperature [53], in contrast with other 2D electron systems [81].
It has been recently demonstrated that the topologically protected surface states can be destroyed by means of Bi to In substitution in (Bi$_{1-x}$In$_x$)$_2$Se$_3$ thin films, determining a Quantum Phase Transition (QPT) from a topological to a trivial insulating phase [82]. Indium substitution, indeed, weakens the spin-orbit interaction causing, in the region between $x(In) = 0.03$ and 0.07, the removal of the valence band-conduction band inversion at the Γ point (see Fig.2), which is at the origin of the Dirac surface state bands. During this transition process, angle-resolved photoemission spectroscopy measurements have shown the closing and the re-opening of the insulating gap Δ in concomitance with the apparence of a "trivial insulating" phase [82].

The trivial phase in (Bi$_{1-x}$In$_x$)$_2$Se$_3$ is characterized by an insulating gap $\Delta \sim 300$ meV (*i.e.* on the same order of magnitude of Bi$_2$Se$_3$) and an extrinsic conduction of massive (Schrödinger) electrons, with density similar to that of Dirac carriers present in the topological phase [82]. In order to discuss the topological protection in the low-energy electrodynamics of 3D topological insulator, we have studied both the single-particle and the plasmon absorption in a ribbon array of (Bi$_{1-x}$In$_x$)$_2$Se$_3$ *vs.* the In content.

In Fig.12a we show a sketch of the THz experiment. A SEM image of a ribbon array for W= 8 μm is shown in Fig. 12b. In Fig. 12c (d) we plot data for light polarization parallel (perpendicular) to the ribbons at different In content. These data have been fitted through a Drude-Lorentz model (black line) and the single components are represented in the same Figure by a blue and green curves for the phonons and by a red-dashed curve for the Drude term. By increasing the In content one observes a reduction of the Drude spectral weight and a broadening of its spectral shape. A similar effect can be observed in Fig. 12d where the plasmon absorption (orange empty circles) is shown together with the Fano fit (black line, see Section 3a) and the bare plasmon (red curve) component.

In order to quantify the effect of In substitution, we report the plasmon broadening Γ_p in Fig.13 (red circles), where the Drude single particle scattering rate Γ_D (as extracted from the present experiment and literature [83]) is also displayed (full and empty blue squares, respectively). As one can clearly see from the Fig.13, the Drude scattering rate Γ_D increases smoothly for low In substitutions ($x \leq 0.04$), consistently with an increased impurity scattering. However, around x =0.04 this smooth trend converts into a steep increase, not explicable in terms of a pure disorder effect due to In substitution. Moreover, this jump is not associated to a lattice transition since the crystal structure of (Bi$_{1-x}$In$_x$)$_2$Se$_3$ does not change in the In interval we studied [82]. This sudden broadening of the Drude term across the QPT has been addressed to the loss of topological protection [61, 83]. Indeed this protection, which is associated with the spin-momentum locking mechanism [84], sets to zero the backscattering probability and it is also effective in reducing the scattering effect (and then the dispersion of single-electron momentum) in a wide range of scattering angles between 100°-180° [85].

The plasmon scattering rate Γ_p shows the same sudden increase across the QPT (Γ_p, passing from 2 THz for $x=0.03$ to 3.1 THz for $x=0.07$). This behavior perfectly follows the single particle one, indicating that the plasmon lifetime mechanism, at least at W= 8 μm, is mainly determined by ohmic losses. Although, one should study the behavior of Dirac plasmon at different wavevectors across the QPT and the QPT mechanism itself should be better clarified in terms of single-particle and collective excitations, the result reported in Fig. 13 strongly suggests that also Dirac plasmons on TIs surface, are topologically protected.

This protection mechanism is particularly promising for quantum plasmonic applications, since it could open a viable path towards long quantum coherence time of plasmon states even at room temperature, if all other plasmon decay channels can be carefully controlled and possibly reduced.

7. CONCLUSION AND PERSPECTIVES.

In this Review, we report on the plasmonic excitations as measured in MBE thin film patterned structures of Bi_2Se_3 topological insulators . We have shown different examples of plasmon structures fabricated from Bi_2Se_3 thin films and discussed their properties. In particular, we have demonstrated that plasmon excitations at the surface of Bi_2Se_3 are mainly due to massless Dirac carriers with a small, less than 10%, co-partecipation of massive Schrodinger charge carriers due to band-bending and accumulation layer effects. The nature of plasmon modes and their spectral shape depend on the geomet-rical micro/nano structure fabricated on the Bi_2Se_3 surface and on an intrinsic interaction between plasmons and phonons *via* a Fano mechanism. Moreover, the non-trivial topology of Bi_2Se_3 characterized by the spin-momentum locking determines a back-scattering protection of both single-particle and plasmon modes, which corresponds to an effective reduction of scattering and to an increase of lifetime of excitations based on Dirac charge-carriers. Finally, the strong dependence of plasmon modes in Bi_2Se_3 on the magnetic field promises a viable path for using them in (terahertz) magneto-optics devices.

The recent observation of a strong non-linear terahertz response of unpatterned Bi_2Se_3 films [86–88] indicating a harmonic generation process due to Dirac electrons, suggests that both the Dirac plasmon long lifetime and their field enhancement could be used for increasing the harmonic generation efficiency, as theoretically predicted [89], and for producing terahertz supercontinuum light in plasmon devices based on topological insulator materials.
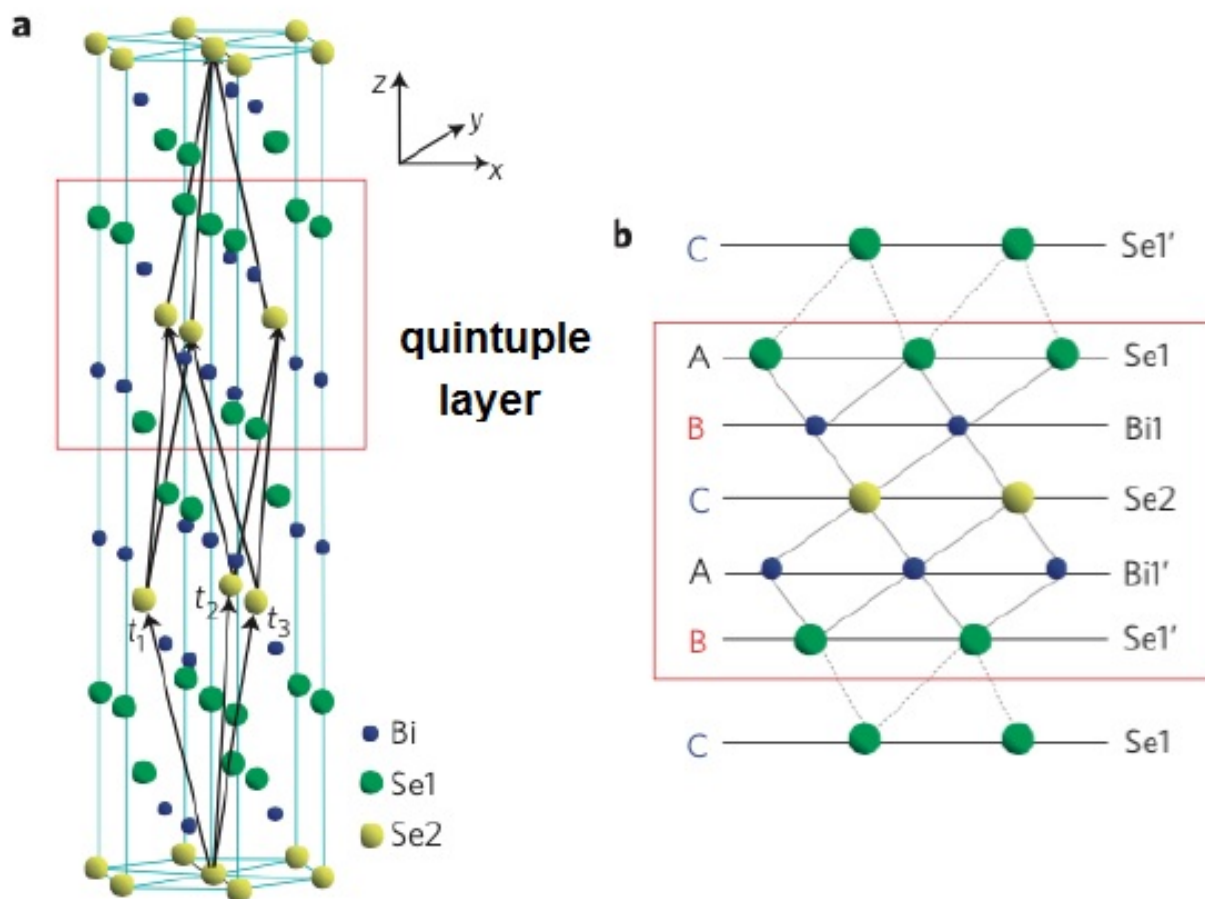
FIG. 1: Crystal structure of Bi_2Se_3. Bi, Se atoms (1 and 2 suffix describe different lattice sites), are indicated by black, green, and yellow circles. The Quintuple Layer unity is indicated by a red box. This figure is adapted from Ref. [59].
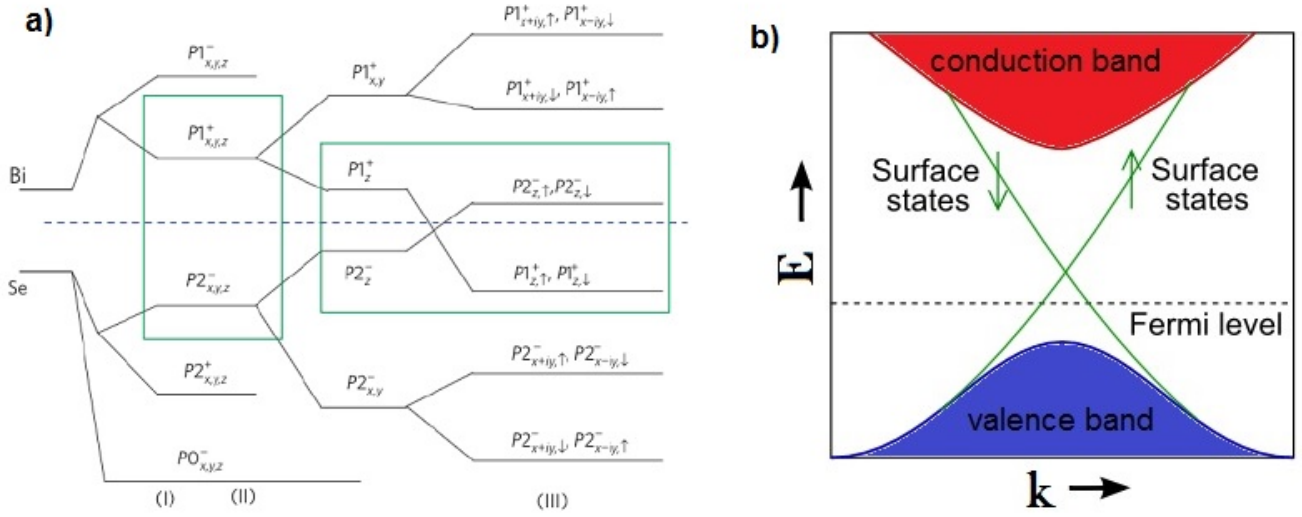
FIG. 2: a. The electronic structure of Bi$_2$Se$_3$. $P1_z^+$ and $P2_z^-$ bands are inverted by the spin-orbit interaction and this inversion determines the non-trivial topology of Bi$_2$Se$_3$. This figure is adapted from Ref. [59]. b. Energy-momentum-dispersion of Bi$_2$Se$_3$. Bulk conduction band are in red and bulk valence band are in blue. The green line represent the spin-polarized linear Dirac surface bands.
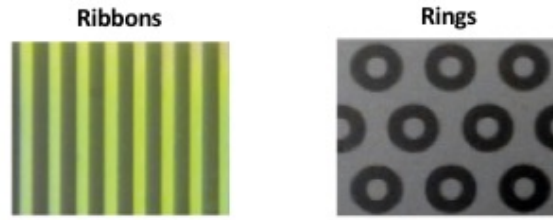
FIG. 3: The two plasmonic microstructures fabricated on Bi$_2$Se$_3$ thin films and studied in this paper. Left: Parallel ribbon array. Rigth: Ring array on an exagonal lattice.
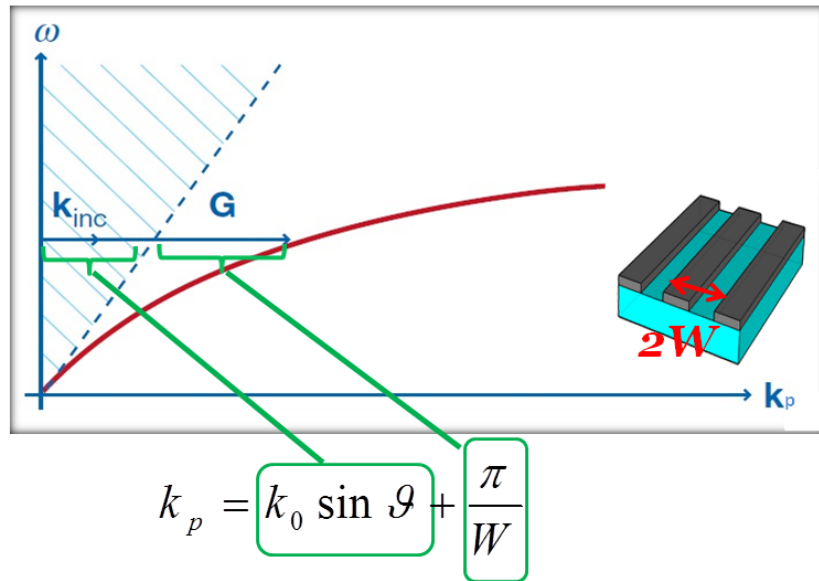
FIG. 4: Frequency-wavevector dispersion of a 2D plasmon (red line). The blue dashed line represents the ligth dispersion. The extrawavevector G needed to excite the plasmon in a photon absorption process is also shown. In the case of a ribbon array of period $L = 2W$ and width W (see inset) the extrawavevector is $k = \pi/W$.
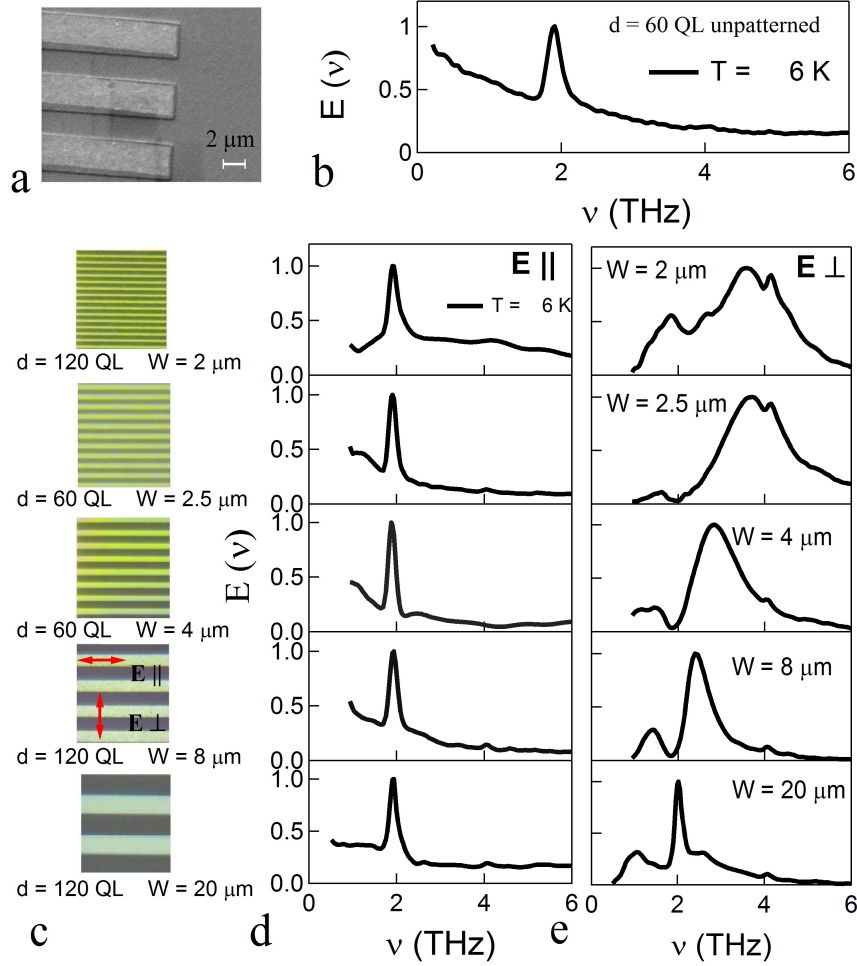
FIG. 5: a) Scanning Electron Microscope (SEM) image of the W=2.5 μm patterned film. b) Extinction coefficient ($E(\nu)$) of the as-grown, unpatterned film, at 6 K (black line). c) Optical-microscope images of the four patterned films with different widths W and periods $2W$; the red arrows indicate the direction of the radiation electric field $\vec{E}$, either perpendicular or parallel to the ribbons. The film thickness is reported under the images where 1 QL$\simeq$ 1 nm. d) Extinction coefficient at 6 K (black lines) of the five patterned films, with the radiation electric field parallel to the ribbons. e) Extinction coefficient of the five patterned films, with the radiation electric field perpendicularly to the ribbons, at 6 K (black lines). All data are normalized by their respective peak values.
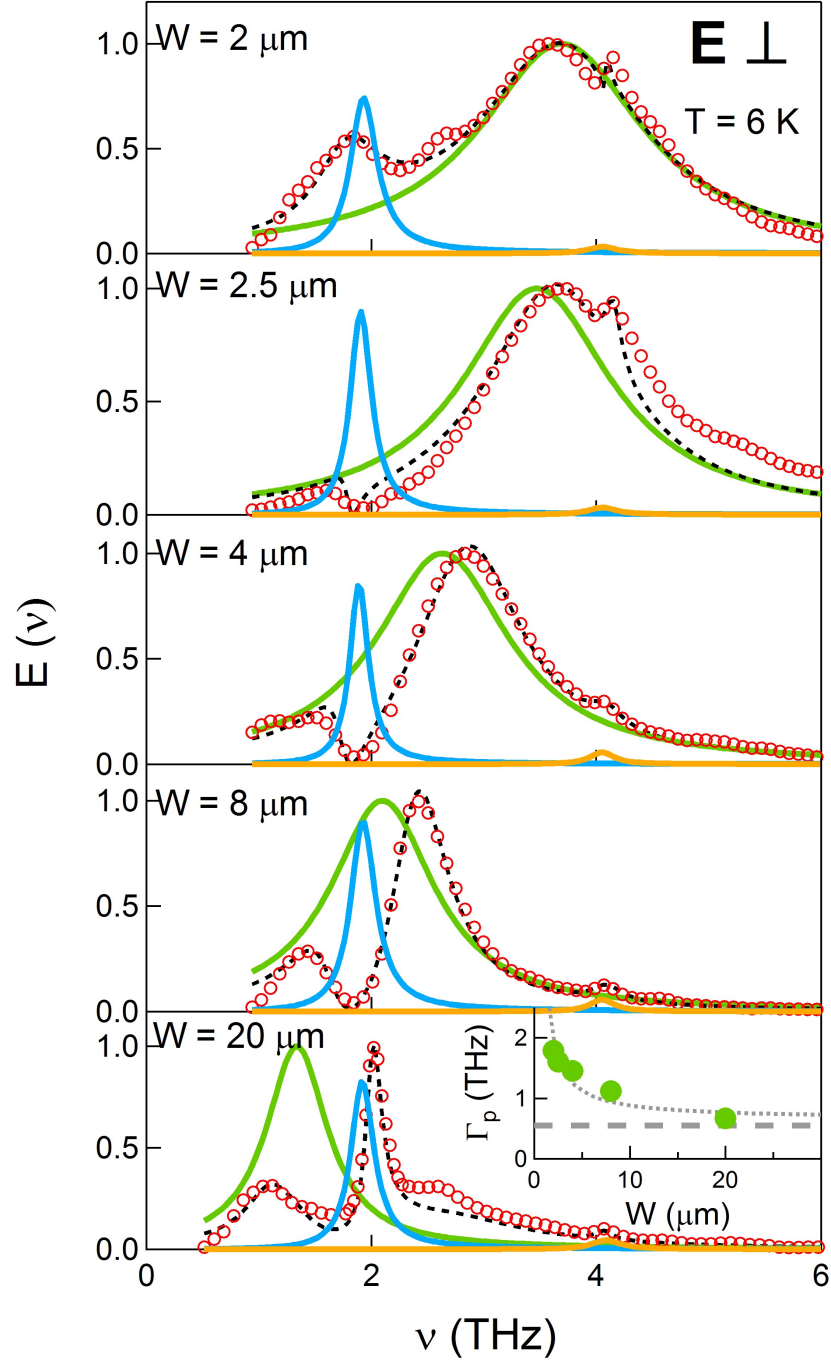
FIG. 6: Extinction coefficient ($E(\nu)$) vs. frequency (ν) of the five patterned films in Fig.5, for the radiation electric field $\vec{E}$ perpendicularly to the ribbons, at 6 K (red circles) and fits to Eq. 1 (black dashed lines). The bare plasmon and phonon contributions, extracted through the fits, are reported by the green and blue line, respectively. The inset in the bottom panel displays the plasmon linewidth Γ_p vs. the ribbon width W at 6 K.
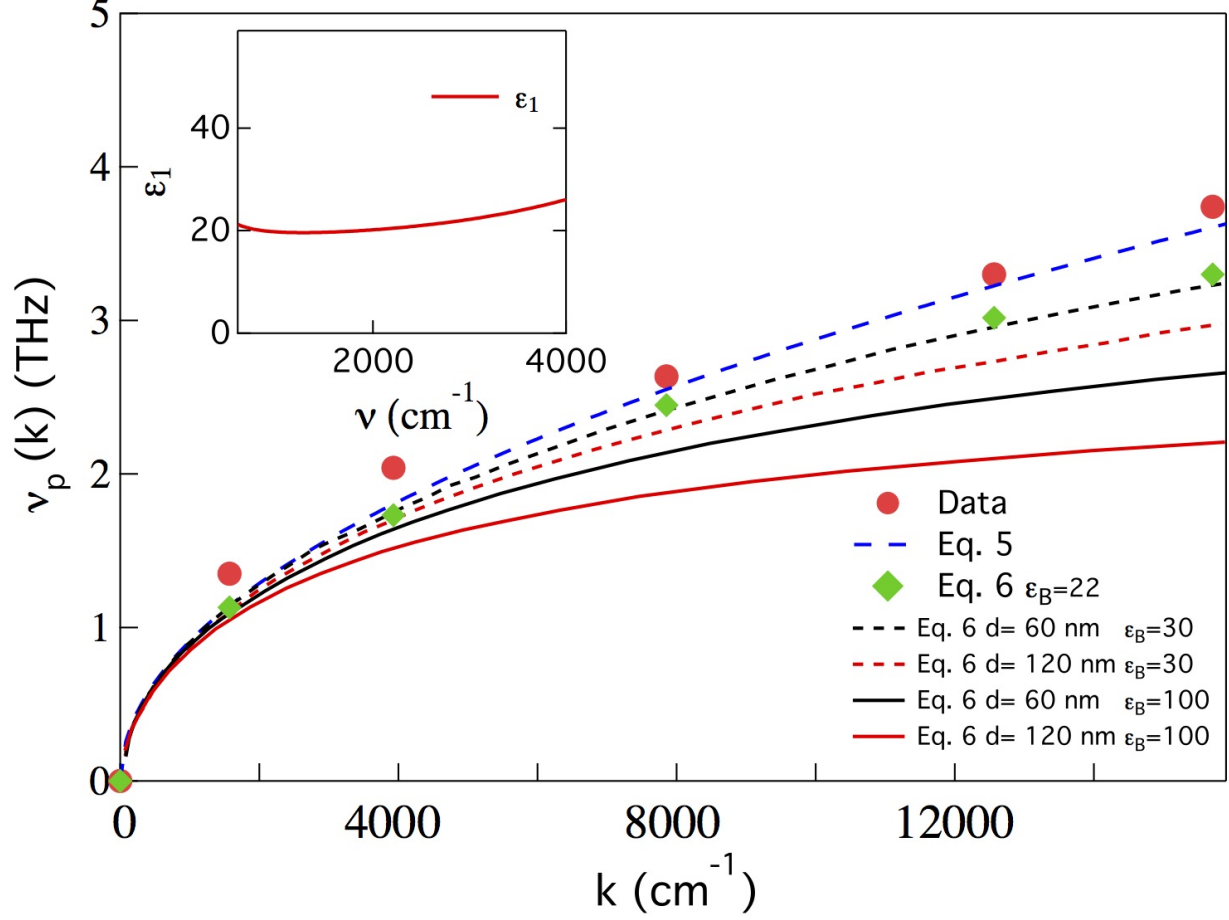
FIG. 7: Experimental values of the plasmon frequency ν_p (red full circles) *vs.* plasmon wavevectors k at 6 K compared with the plasmon dispersion for Dirac plasmon (blue dashed line), calculated in the low-k limit with no free parameters by Eq. 5 (see text). A very good superposition among experimental and theoretical data exists in this approximation limit. In the same Figure we report calculations as obtained from Eq. 6 (see text), which takes into account the bulk dielectric contribution in the plasmon dispersion. Black dashed (60 QL thick film) and red dashed (120 QL thick film) lines are calculated for $\epsilon_{bulk}=$ 30 [70]. Continous black and red lines for $\epsilon_{bulk}=$ 100 [70]. Green diamonds represent the calculation by Eq. 6 for the actual bulk dielectric function whose value ($\epsilon_{bulk}=22$), is reported in the inset. The good comparison among data and calculation for $\epsilon_{bulk}=22$ indicates that the main contribution to plasmon excitations at the surface of Bi_2Se_3 comes from Dirac carriers. The small disagreement (underestimate), less than 10% at the highest wavevector, suggests a possible small role of massive surface electrons.
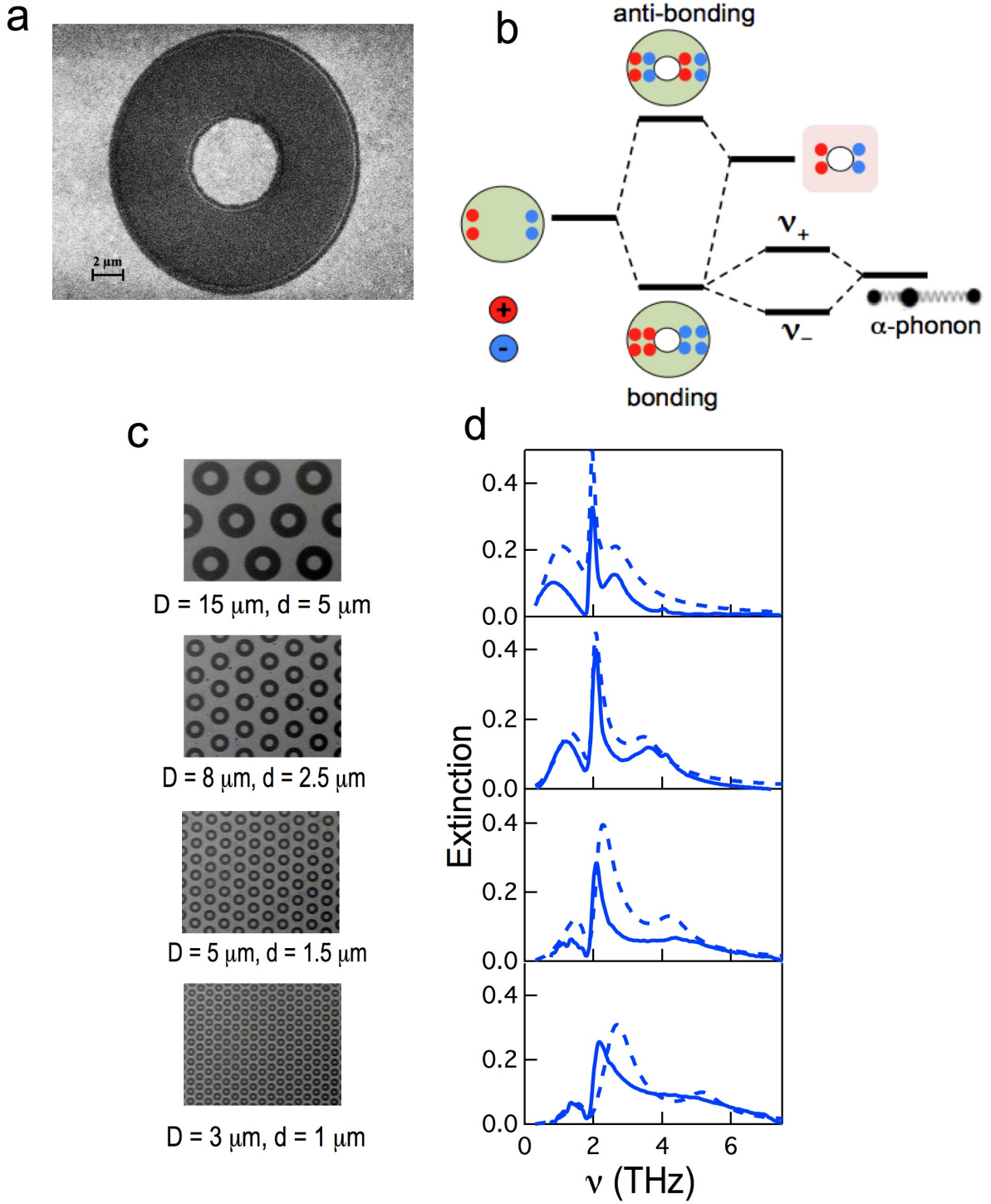
FIG. 8: a) A SEM image of the D=15 μm patterned film. b) The optical microscope images of the different ring arrays measured in this paper. c) The extinction spectra of the ring-arrays at 10 K. The two peaks structure at low-frequency can be explained in terms of the hybridization of the bonding ring plasmon and the α bulk phonon. The high frequency peak corresponds to the antibonding plasmon. d) The charge distribution of bonding and antibonding plasmons in a ring.
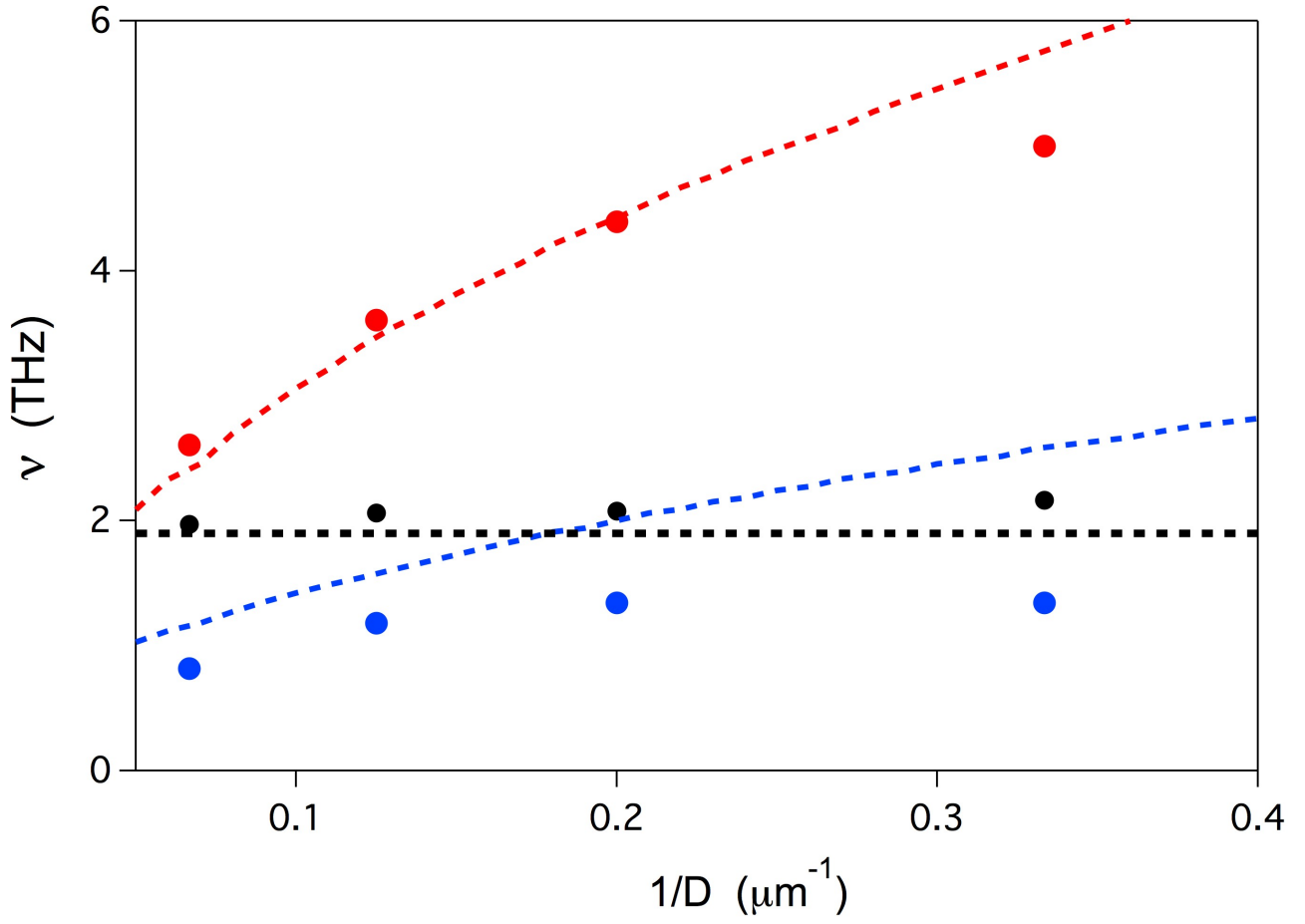
FIG. 9: The bare plasmon frequencies (blue circles for the bonding mode and red circles for the antibonding one), extracted through a Fano fit, *vs.* $1/D$, a parameter which has the meaning of the "average" extrawave-vector needed to activate the photon absorption process. The bare bonding mode cross the phonon frequency (black-dashed horizontal line) and these two modes interacts through a Fano mechanism. In contrast, the antibonding plasmon, always higher in frequency than the phonon mode, has a negligeble Fano interaction.
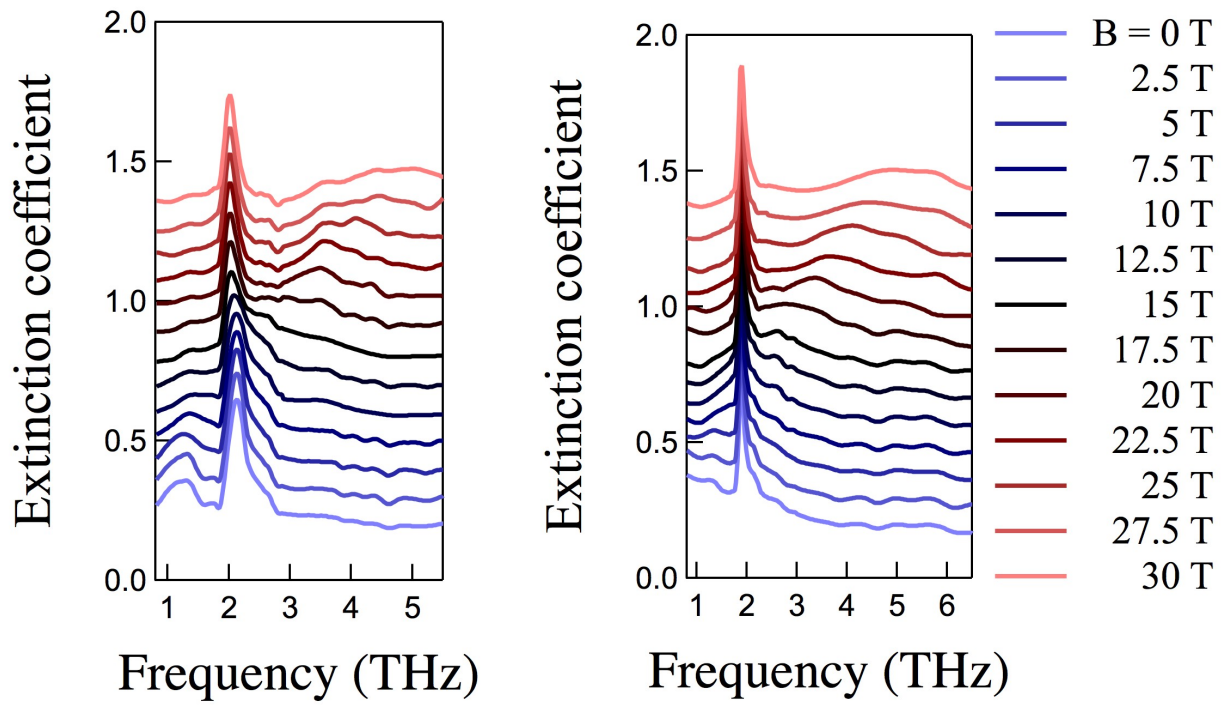
FIG. 10: a) Extinction spectra for Bi$_2$Se$_3$ ribbon arrays with light polarized perpendicular to the ribbons which provides the plasmon excitation *vs.* the magnetic field B from 0 to 30 T. b) Extinction spectra for light polarized parallel to the ribbons providing the single-particle excitations at the same fields. Subsequent increasing field spectra are shifted in intensity by a factor +0.1 to better display the behavior of excitations. For increasing B one observes a hardening of both the magnetoplasmon and cyclotron resonance.
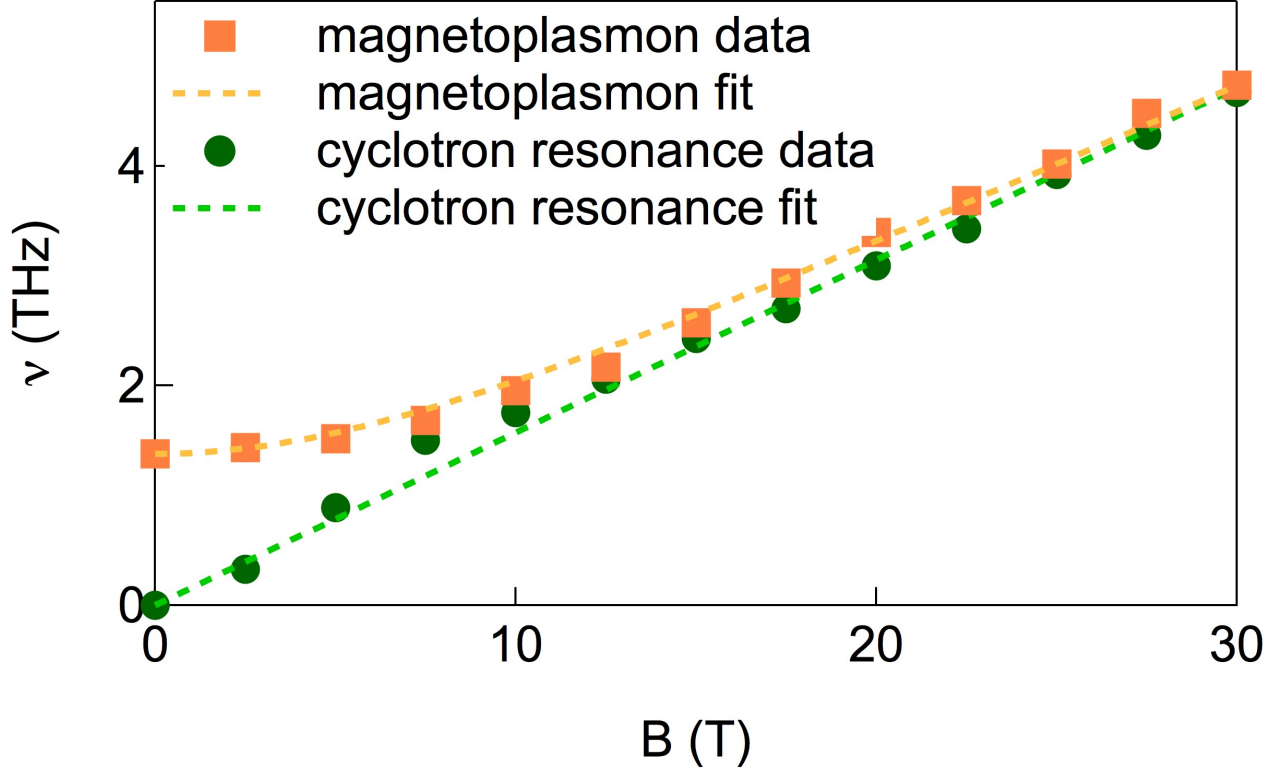
FIG. 11: Experimental magnetoplasmon (orange squares) and cyclotron frequencies (green circles) *vs*. B, as extracted from a Fano (Drude-Lorentz) fit of the extinction spectra of Bi_2Se_3 ribbon arrays shown in Fig.10a and b. The magnetoplasmon and cyclotron dispersions fitted to Eq. 6 and 7, respectively, provides both a dynamical Dirac mass $m_D^*=0.18\pm0.01\ m_e$.
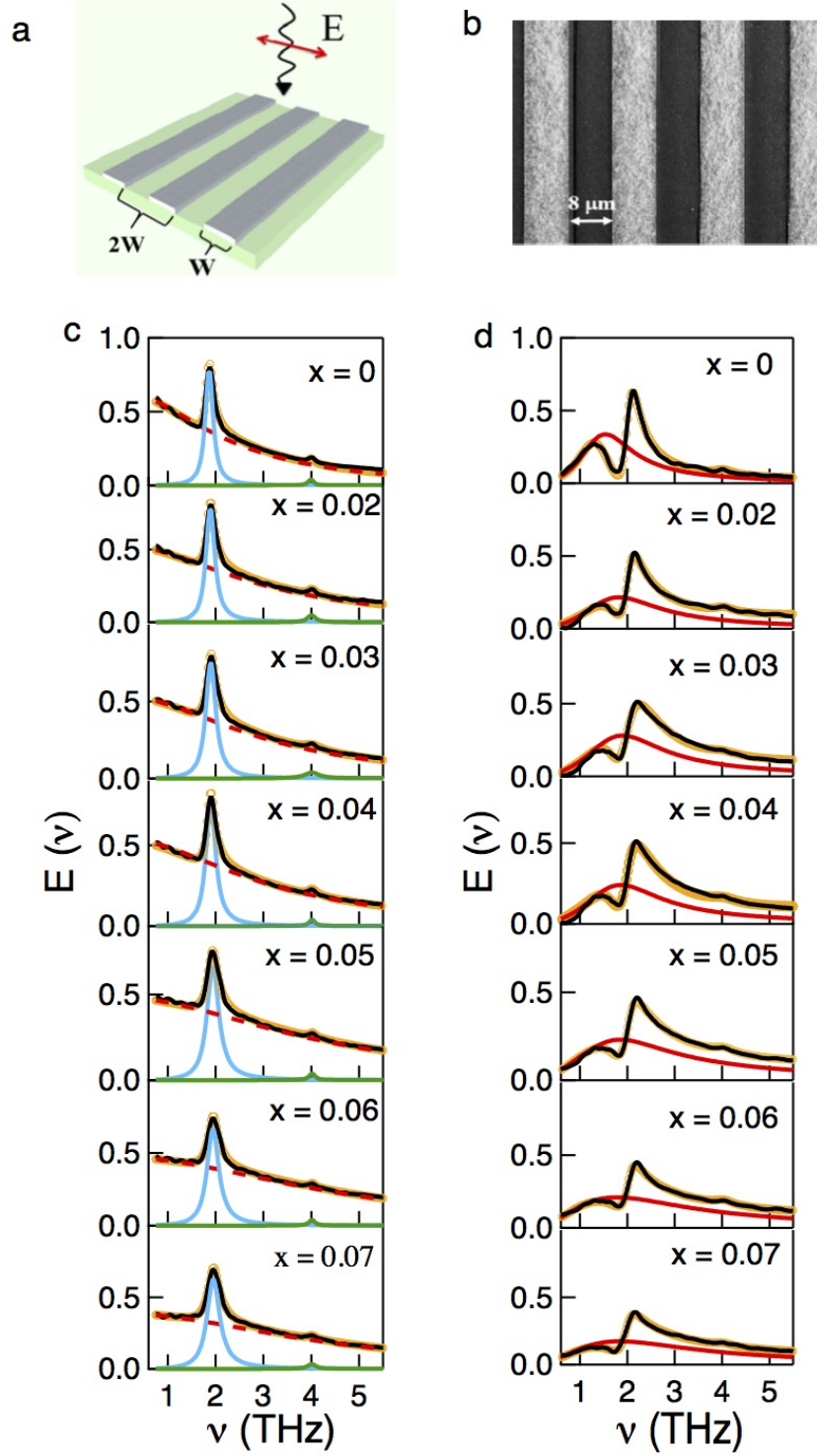
FIG. 12: a) SEM image of the ribbon array patterned $x = 0$ film. b) Optical scheme of the THz experiment. c) Experimental extinction spectra at 10 K for unpatterned $(Bi_{1-x}In_x)_2Se_3$ thin films (orange empty circles). Drude-Lorentz model fitting for the conductance (black line). The different contributions in the Drude-Lorentz fit are shown separately: Drude term (red dashed line), α- (green) and β-phonon (purple). d) Extinction spectra (orange empty circles) for ribbon array patterned ($W = 8\mu m$) films, with light polarization perpendicular to the ribbons. Fano fit for plasmon-phonon interaction (black lines) at 10 K. The bare plasmon curve is represented as a red line.
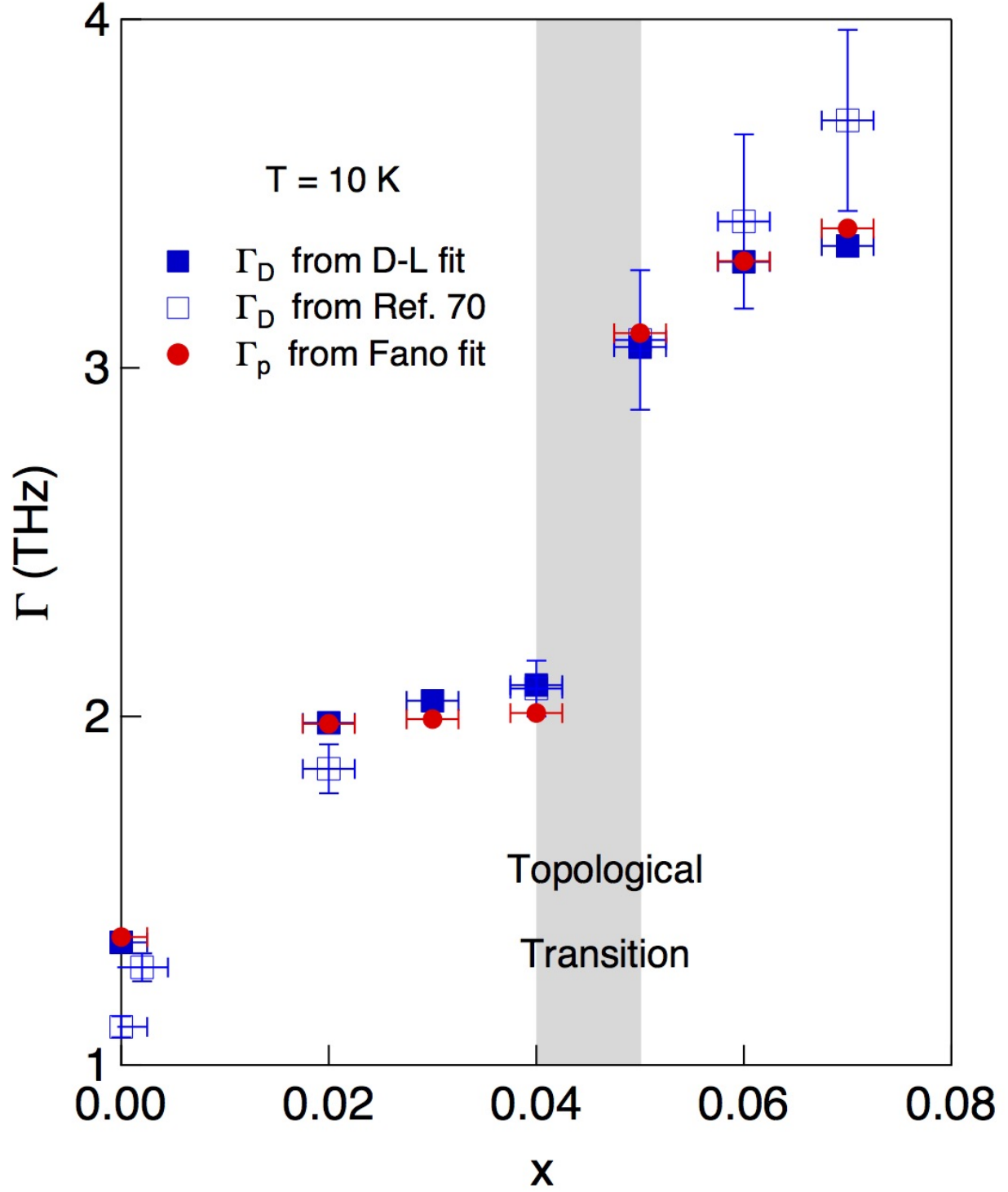
FIG. 13: Comparison between the plasmon scattering rate Γ_p (red circles) and Drude scattering rate Γ_D from the present experiment (blue squares) and literature [83] (blue empty squares), versus In content x at T=10 K. A sudden broadening of both scattering rates can be observed across the QPT transition represented as a gray region.

REFERENCES

[1] Maier S. A. *Plasmonics: fundamentals and applications.* *Springer-Verlag, New York,* (2007).

[2] K.-S. Lee, *et al.* Gold and silver nanoparticles in sensing and imaging: Sensitivity of plasmon response to size, shape, and metal composition. *J. Phys. Chem. B* **110**, 19220-19225 (2006).

[3] J. N. Anker, *et al.* Biosensing with plasmonic nanosensors. *Nat. Mater.* **6**, 442–453 (2008).

[4] O. Limaj, *et al.* Field distribution and quality factor of surface plasmon resonances of metal meshes for mid-infrared sensing. *Plasmonics* **10**, 45–50 (2015).

[5] F. D'apuzzo, *et al.* Resonating Terahertz Response of Periodic Arrays of Subwavelength Apertures. *Plasmonics* **8**, 851–858 (2013).

[6] O. Limaj, *et al.* Midinfrared surface plasmon sensor based on a substrateless metal mesh. *App. Phys. Lett.* **117**, 091902–091905 (2011).

[7] O. Limaj, *et al.* Mid-Infrared Surface Plasmon Polariton Sensors Resonant with the Vibrational Modes of Phospholipid Layers. *Jornal of Phys. Chem. C* **98**, 19119–19126 (2013).

[8] A. Toma, *et al.* Squeezing Terahertz Light into Nanovolumes: Nanoantenna Enhanced Terahertz Spectroscopy (NETS) of Semiconductor Quantum Dots. *Nano Letters* **15**, 386–391 (2015).

[9] D. E. Chang, *et al.* Quantum optics with surface plasmons. *Phys. Rev. Lett.* **97**, 053002 (2006).

[10] A. V. Akimov, *et al.* Generation of single optical plasmons in metallic nanowires coupled to quantum dots. *Nature* **450**, 402–406 (2007).

[11] M. Danckwerts, *et al.* Optical frequency mixing at coupled gold nanoparticles. *Phys. Rev. Lett.* **98**, 026104 (2007).

[12] A. R. Davoyan, *et al.* Nonlinear plasmonic slot waveguide. *Opt. Expr.* **16**, 21209–21214 (2008).

[13] H. A. Atwater, *et al.* Plasmonics for improved photovoltaic devices. *Nat. Mater.* **9**, 205–213 (2010).

[14] D. P. O'Neal, *et al.* Photo-Thermal Tumor Ablation in Mice Using Near Infrared-Absorbing Nanoparticles. *Cancer Lett.* **209**, 171–176 (2004).

[15] P. K. Jain, *et al.* Au nanoparticles target cancer. *Nanotoday* **2**, 18–29 (2007).

[16] S. Link, *et al.* Spectral Properties and Relaxation Dynamics of Surface Plasmon Electronic Oscillations in Gold and Silver Nanodots and Nanorods. *J. Phys. Chem. B* **103**, 8410-8426 (1999).

[17] S. Lupi, *et al.* Fano effect in the a-b plane of $Nd_{1.96}Ce_{0.04}CuO_{4+y}$: Evidence of phonon interaction with a polaronic background. *Phys. Rev. B* **57**, 1248-1252 (1998).

[18] S. Lupi, *et al.* Infrared active aibrational-modes strongly coupled to carriers in high-Tc superconductors. *Europhys. Lett.* **31**, 473-478 (1995).

[19] P. Nordlander, *et al.* Plasmon hybridizaton in nanoparticle dimers. *Nano Lett.* **4**, 899–903 (2004).

[20] L. Gunnarsson, *et al.* Confined plasmons in nanofabricated single silver particle pairs: Experimental observations of strong interparticle interactions. *J. Phys. Chem. B* **109**, 1079–1087 (2005).

[21] L. M. Liz-Marzán Tailoring surface plasmon through the morphology and assembly of metal nanoparticles. *Langmuir* **22**, 32–41 (2006).

[22] A. Taleb, *et al.* Optical properties of self-assembled 2D and 3D superlattices of silver nanoparticles. *J. Phys. Chem. B* **102**, 2214–2220 (1998).

[23] P. S. Kumar, *et al.* High-yield synthesis and optical response of gold nanostars. *Nanotechnology* **19**, 015606 (2008).

[24] R. D. Averitt, *et al.* Plasmon resonance shifts of Au-coated Au_2S nanoshells: Insight into multicomponent nanoparticle growth. *Phys. Rev. Lett.* **78**, 4217–4220 (1997).

[25] M. Grzelczak, *et al.* Shape control in gold nanoparticle synthesis. *Chem. Soc. Rev.* **37**, 1783–1791 (2008).

[26] J. Aizpurua, *et al.* Optical properties of gold nanorings. *Phys. Rev. Lett.* **90**, 057401 (2003).

[27] E. Prodan, *et al.* A Hybridization Model for the Plasmon Response of Complex Nanostructures. *Science* **302**, 419-422 (2003).

[28] Z. Fang, *et al.* Gated tunability and hybridization of localized plasmons in nanostructured graphene. *ACS Nano* **7**, 2388 (2013).

[29] O. Limaj, *et al.* Superconductivity-induced transparency in terahertz metamaterials. *ACS Photonics* **1**, 570–575 (2014).

[30] S. Zhang, *et al.* Plasmon-induced transparency in metamaterials. *Phys. Rev. Lett.* **101**, 047401 (2008).

[31] J. B. Khurgin, How to deal with the loss in plasmonics and metamaterials. *Nat. Nanotech.* **10**, 2 (2015).

[32] A. Brandstetter-Kunc, *et al.* Nonradiative limitations to plasmon propagation in chains of metallic nanoparticles. *ArXiv:1697.02999 preprint* **2**, 2 (2016).

[33] G. V. Naik, *et al.* Alternative plasmonic materials: beyond gold and silver. *Adv. Mater.* **25**, 3264–3294 (2013).

[34] B. Wunsch, *et al.* Dynamical polarization of graphene at finite doping. *New J. Phys.* **8**, 318 (2006).

[35] A. Bostwick, *et al.* Dynamical polarization of graphene at finite doping. *Nat. Phys.* **3**, 36–40 (2007).

[36] Z. Fei, *et al.* Gate-tuning of graphene plasmons revealed by infrared nano-imaging. *Nature* **487**, 82–85 (2012).

[37] J. Chen, *et al.* Optical nano-imaging of gate-tunable graphene plasmons. *Nature* , advance online publication (2012).

[38] V. W. Brar, *et al.* Highly confined tunable mid-infrared plasmonics in graphene nanoresonators. *Nano Lett.* **13**, 2541-2547 (2013).

[39] Z. Fei, *et al.* Infrared nanoscopy of Dirac plasmons at the graphene–SiO_2 interface. *Nano Lett.* **11**, 4701–4705 (2011).

[40] L. Ju, *et al.* Graphene plasmonics for tunable terahertz metamaterials. *Nat. Nanotech.* **6**, 630–634 (2011).

[41] K. F. Mak, *et al.* Measurement of the optical conductivity of graphene. *Phys. Rev. Lett.* **101**, 196405 (2008).

[42] K. S. Novoselov, *et al.* Electric field effect in atomically thin carbon films. *Science* **306**, 666–669 (2004).

[43] K. S. Novoselov, *et al.* Two-dimensional gas of massless Dirac fermions in graphene. *Nature* **438**, 197–200 (2005).

[44] Hasan, M. Z. & Kane, C. L. *Colloquium* : Topological insulators. *Rev. Mod. Phys.* **82**, 3045–3067 (2010).

[45] Kane, C. L. & Mele, E. J. Quantum spin hall effect in graphene. *Phys. Rev. Lett.* **95**, 226801 (2005).

[46] Moore, J. E. The birth of topological insulators. *Nature* **464**, 194 (2010).

[47] Fu, L. & Collins, G. P. Computing with quantum knots. *Sci. Am.* **294**, 57 (2006).

[48] Kitaev, A. & Preskill, J. Topological entanglement entropy. *Phys. Rev. Lett.* **96**, 110404 (2006).

[49] Zhang, X., Wang, J. & Zhang, S.-C. Topological insulators for high-performance Terahertz to infrared applications. *Phys. Rev. B* **82**, 245107 (2010).

[50] Chen, Y. *et al.* Experimental realization of a three-dimensional topological insulator, Bi_2Te_3. *Science* **325**, 178 (2009).

[51] Raghu, S., *et al.*, Collective Modes of a Helical Liquid. *Phys. Rev. Lett.* **104**, 116401 (2010).

[52] Valdes Aguilar, R., *et al.*, THz response and colossal Kerr rotation from the surface states of the topological insulator Bi_2Se_3. *Phys. Rev. Lett.* **108**, 087403 (2012).

[53] Di Pietro, P. *et al.* Observation of Dirac plasmons in a topological insulator. *Nature Nanotechnology* **8**, 556 (2013).

[54] M. Autore, *et al.* Plasmon-Phonon Interactions in Topological Insulator Microrings. *Adv. Opt. Mat.* **3**, 1257-1263 (2015).

[55] M. Autore, *et al.* Observation of Magnetoplasmons in Bi_2Se_3 Topological Insulator. *ACS Phot.* **2**, 1231-1235 (2015).

[56] M. Autore, *et al.* Topologically protected Dirac plasmons and their evolution across the quantum phase transition in a $(Bi_{1?x}In_x)_2Se_3$ topological insulator. *Nanoscale* **8**, 4667-4671 (2016).

[57] A. Politano, *et al.* Interplay of Surface and Dirac Plasmons in Topological Insulators: The Case of Bi_2Se_3. *Phys. Rev. Lett.* **115**, 216802 (2015).

[58] Bansal, N., Kim, Y. S., Brahlek, M., Edrey, E. & Oh, S. Thickness-independent transport channels in topological insulator Bi_2Se_3 thin films. *Phys. Rev. Lett.* **109**, 116804 (2012).

[59] Zhang, H.J. *et al.* Topological insulators in Bi_2Se_3, Bi_2Te_3 and Sbi_2Te_3 with a single dirac cone on the surface.. *Nature Phys.* **5**, 438 (2009).

[60] Black, E.M. *et al.* Bismuth sulfide (Bi_2Se_3) optical properties, dielectric constants. *J. Phys. Chem. Solids* **2**, 240 (1957).

[61] Bansal, N., *et al.*, Epitaxial growth of topological insulator Bi_2Se_3 thin film on Si(111) with atomically sharp interface. *Thin Solid Film* **520,**, 224 (2011).

[62] Ju, L. *et al.* Graphene plasmonics for tunable Terahertz metamaterials. *Nat Nano* **6**, 630 (2011).

[63] Allen, S. J., Tsui, D. C. & Logan R. A. Observation of the two-Dimensional plasmon in Silicon Inversion Layers. *Phys. Rev. Lett.* **38**, 980–983 (1977).

[64] Di Pietro, P. *et al.* Optical conductivity of bismuth-based topological insulators. *Phys. Rev. B* **86**, 4701 (2012).

[65] Fei, Zhe *et al.* Infrared Nanoscopy of Dirac Plasmons at the Graphene-SiO_2 interface. *Nano Lett.* **11**, 4701 (2011).

[66] Giannini, V., Francescato, Y., Amrania, H., Phillips, C. C. & Maier, S. A. Fano resonances in nanoscale plasmonic systems: A parameter-free modeling approach. *Nano Lett.* **11**, 2835 (2011).

[67] Profumo, R.E.V. *et al.* Double-layer graphene and topological insulator thin-film plasmons. *Phys. Rev. B,* **85**, 085443 (2012).

[68] Das Sarma, S. & Hwang, E. H. Collective modes of the massless Dirac plasma. *Phys. Rev. Lett.* **102**, 206412 (2009).

[69] Cao Yue, *et al.* In-Plane Helical Orbital Texture Switch near the Dirac Point in the Topological Insulator Bi_2Se_3. *http://arxiv.org/abs/1209.1016*

[70] Stauber, T. & et al. Spin-charge separation of plasmonic excitations in thin topological insulators. *Phys. Rev. B* **88**, 205427 (2013).

[71] Stauber T., Plasmonics in dirac systems: from graphene to topological insulators. *Journal of Physics: Condensed Matter* **26**, 123201 (2014).

[72] Kuzmenko A.B. Guide to Reffit: software to fit optical spectra, 2004, available online at: http://optics.unige.ch/alexey/reffit.html;

[73] Wu, L. & et al. High-Resolution Faraday Rotation and Electron-Phonon Coupling in Surface States of the Bulk-Insulating Topological Insulator $Cu_{0.02}Bi_2Se_3$. *Phys. Rev. Lett.* **115**, 217602 (2015).

[74] Sim S., *et al.* Ultra-high modulation depth exceeding 2,400% in optically controlled topological surface plasmons. *Nat. Commun.* **6**, 8814 (2015).

[75] S. Thongrattanasiri, *et al.* Gated tunability and hybridization of localized plasmons in nanostructured graphene. *Phys. Rev. Lett.* **108**, 047401 (2012).

[76] L. D. Landau and E.M. Lifshitz *Quantum Mechanics, Course of Theoretical Physics. Volume 3. Pergamon* (1965).

[77] D. J. Hilton "Cyclotron Resonance" in: *Characterization of Materials. John WileySons, New York* (2012).

[78] I. V. Kukushkin, *et al.* Collective excitations in two-dimensional electron stripes: transport and optical detection of resonant microwave absorption. *Phys. Rev. B* **73**, 113310 (2006).

[79] G. Armelles, *et al.* Combining Magnetic and Plasmonic Functionalities. *Adv. Opt. Mat.* **1**, 10?35 (2013).

[80] V.A. Volkov *et al.* Edge magnetoplasmons: low frequency weakly damped oscillations in inhomogeneous two-dimensional electron systems. *Zh. Eksp. Teor. Fiz.* **94**, 217-241 (1988).

[81] S. J. Allen, *et al.* Observation of the Two-Dimensional Plasmon in Silicon Inversion Layers. *Phys.Rev. Lett.* **38**, 980 (1977).

[82] M. Brahlek, *et al.* Topological-Metal to Band-Insulator Transition in $(Bi_{1?x}In_x)_2Se_3$ Thin Films. *Phys.Rev. Lett.* **109**, 186403 (2012).

[83] L. Wu, *et al.* A sudden collapse in the transport lifetime across the topological phase transition in $(Bi_{1-x}In_x)_2Se_3$. *Nature Phys.* **9**, 410 (2013).

[84] Y. Ando Topological Insulator Materials. *J. Phys. Soc. Jpn.* **82**, 102001–102032 (2013).

[85] S. Kim, *et al.* Robust Protection from Backscattering in the Topological Insulator $Bi_{1.5}Sb_{0.5}Te_{1.7}Se_{1.3}$. *Phys. Rev. Lett.* **112**, 36802–136805 (2014).

[86] F. Giorgianni, *et al.* Strong nonlinear terahertz response induced by Dirac surface states in Bi_2Se_3 topological insulator. *Nature Commun.* **7**, 1421 (2016).

[87] Chiadroni E., *et al.* Laser comb with velocity bunching: Preliminary results at SPARC. *Nucl. Instrum. Meth. A* **637**, S43–S46 (2011).

[88] Chiadroni E., *et al.* Characterization of the THz radiation source at the Frascati linear accelerator. *Review of Scientific Instruments* **84**, 0227031-02270312 (2013).

[89] Yao X., *et al.* Efficient Nonlinear Generation of THz Plasmons in Graphene and Topological Insulators. *Phys. Rev. Lett.* **112**, 055501 (2014).